

Computational Prediction of Graphdiyne-Supported Three-Atom Single-Cluster Catalysts

Jin-Cheng Liu¹, Hai Xiao¹, Xiao-Kun Zhao¹, Nan-Nan Zhang¹, Yuan Liu^{1,2}, Deng-Hui Xing¹, Xiaohu Yu³, Han-Shi Hu¹ & Jun Li^{1,2*}

¹Department of Chemistry, Key Laboratory of Organic Optoelectronics and Molecular Engineering of the Ministry of Education, Tsinghua University, Beijing, ²Department of Chemistry, Southern University of Science and Technology, Shenzhen, Guangdong, ³Shaanxi Key Laboratory of Catalysis, School of Chemical and Environment Sciences, Shaanxi University of Technology, Hanzhong, Shaanxi

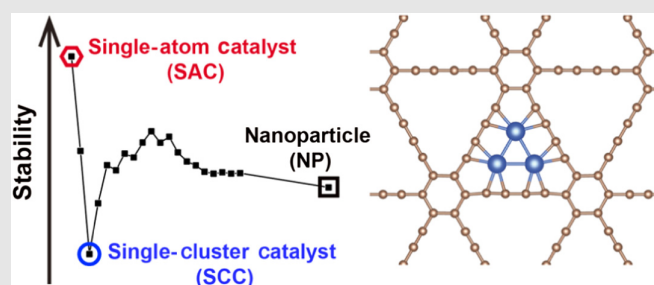
*Corresponding author: junli@tsinghua.edu.cn

Cite this: *CCS Chem.* **2023**, 5, 152–163

DOI: [10.31635/ccschem.022.202201796](https://doi.org/10.31635/ccschem.022.202201796)

While heterogeneous single-atom catalysts (SACs) have achieved great success in the past decade, their application is potentially limited by their simplistic single-atom active centers, which make single-cluster catalysts (SCCs) a natural extension in the domain of heterogeneous catalysis. SCCs with precise numbers of atoms and structural configurations possess SAC merits, yet have greater potential for catalyzing complex reactions and/or bulky reactants. Through systematic quantum-chemical studies and computational screening, we report here the rational design of transition metal three-atom clusters anchored on graphdiyne (GDY) as a novel kind of stable SCC with great promise for efficient and atomically precise heterogeneous catalysis. By investigating their structure and catalytic performance for the oxygen reduction reaction, the hydrogen evolution reaction, and the CO₂ reduction reaction, we have provided theoretical

guidelines for their potential applications as heterogeneous catalysts. These GDY-supported three-atom SCCs provide an ideal benchmark scaffold for rational design of atomically precise heterogeneous catalysts for industrially important chemical reactions.



Keywords: single-cluster catalyst, single-atom catalyst, graphdiyne, atomically precise heterogeneous catalysis

Introduction

In the past decade, single-atom catalysts (SACs) have emerged as the new frontier of heterogeneous catalysis, owing to their high performance with regard to atomic efficiency, selectivity, stability, and activity, as well as precisely tunable quantum states through support manipulation.^{1–5} However, SACs are not always an optimal design for complex reactions, such as those that require multistep

redox reactions (e.g., in photosynthesis and nitrogenase), interaction among two or more adsorbed bulky reactant molecules, or multiple functional sites (e.g., in order to break the cumbersome scaling relations).⁶

Atomic clusters that contain only a small number of atoms can exhibit unique and often unexpected properties for catalytic reactions such that SAC may not work well.^{7–9} The term “cluster” was coined by F.A. Cotton in the early 1960s to refer specifically to compounds

containing metal-metal bonds. Up to now, there are many synthetic strategies of supported atomic clusters for heterogeneous catalysis, for instance, gas-phase mass filters or so-called “soft landing,”¹⁰ the precursor-preselected strategy from the confined effect of zeolitic or MOF frameworks,^{11–13} the host-guest strategy,¹⁴ the wet chemical reduction,¹⁵ the dendrimer-based strategy, and so on.¹⁶ Recently, single-cluster catalysts (SCCs) with atomically precise active centers composed of well-defined stable clusters with constant atomic constitutions and structures have been proposed as a natural extension of SACs for optimal design of complicated heterogeneous catalysts.^{6,10,11,14,17–21} However, the stability and thus the synthesis of SCCs pose a grand challenge because a delicate balance is required to prevent both further aggregation of the clusters to form large size clusters or nanoparticles and their dispersion to form supported single atoms.

To form robust SCCs, a prototype material with natural pores or defect-anchoring sites is necessary. The synthesis of graphdiyne (GDY) by Li et al.^{22–26} presents an ideal substrate for hosting both SACs and SCCs since GDY has natural 6-membered rings (6MRs) and 18-membered rings (18MRs). There have been reports of metal/GDY complexes with various applications,^{27,28} and the 18MR-hole of GDY has been shown to provide a suitable site for anchoring a metal (M) single atom (SA) or single cluster (SC) as a heterogeneous catalyst.²⁹ However, most previous work on M_x/GDY has focused on SAs. For example, nonnoble metal Fe and Ni SAs anchored on GDY (denoted as Fe₁/GDY and Ni₁/GDY) have been shown to perform better in the hydrogen evolution reaction (HER) than in the commercial Pt/C.²⁹ By first-principles calculations, the stability and electronic structures of M₁/GDY with 3d metals (M = Sc – Zn) were systematically investigated in our group.³⁰ Additionally, Mo₁/GDY,³¹ Ir₁/GDY,³² W₁/N-doped GY,³³ Pt₁/GDY,³⁴ Fe₁/GDY,³⁵ AM₁/GDY,³⁶ and TM₁/GDY³⁷ (AM = alkali metal and TM = transition metal) were theoretically proposed as good catalysts for reactions including nitrogen fixation, CO oxidation, HER, oxygen reduction reaction (ORR), and water splitting.

However, these studies on M₁/GDY did not explore the possibility that the SA form of metal on GDY might be less stable than its SC form, particularly when compared with the highly stable triatomic cluster form.^{38,39} Ma et al.⁴⁰ reported diatomic cluster catalysts on GDY for nitrogen reduction reaction. Zhang et al.⁴¹ speculated that the triangular 18MR-hole of GDY can accommodate three Li atoms at the three symmetric corners with a unique triangular configuration, and the resulting Li₃/GDY can be used as anode material for lithium ion batteries. Qi et al.⁴² investigated the performance of Pd clusters on GDY for catalytic reduction but did not characterize the structure of Pd clusters. Very recently, we showed that the Os₃/GDY and its analogs are a class of potential catalyst for selective semihydrogenation of acetylene.⁴³ Moreover, we predicted that the M₃ form is indeed the most stable for

Pt and Ni supported on GDY and suggested an efficient strategy based on the electrochemical potential window (EcPW) to prepare them via an electrochemical route.³⁹

The metal trimer SCCs have been reported to deliver excellent performance. Based on Ji et al.’s reported experimental work, the Ru₃ cluster supported on N-doped carbon material was shown to be an efficient catalyst for selective oxidation of alcohols.¹¹ The Ag₃ cluster on alumina support was demonstrated with high activity and selectivity for direct propylene epoxidation.¹⁸ The [Cu₃(μ -O)₃]²⁺ cluster in mordenite was shown to exhibit high reactivity towards activation of inert C-H bonds in methane.^{21,44} By first-principles calculations, we predicted that the Fe₃ cluster supported on Al₂O₃ leads to an associative mechanism for low-temperature ammonia synthesis with a high turnover frequency.²⁰

However, in addition to the EcPW strategy, our group suggested efficient and specific ways to prepare stable metal trimer SCCs that are still lacking because of the delicate requirement for the interaction between metal and support. On the one hand, when the metal-support bonding is much stronger than the metal-metal bonding, the metal trimer SC will dissociate to form SAs. On the other hand, if the metal-support interaction is much weaker than the metal-metal bonding, the metal trimer SCs will aggregate into bigger clusters or nanoparticles. Thus, it is a prerequisite for a support for hosting the metal trimer SCC to balance the metal-metal and metal-support bonding strengths. In this work, we investigate the viability of GDY as a support for TM trimer SCCs from both thermodynamic and kinetic aspects by first-principles calculations. All in all, we have considered 13 late TM elements for M₃/GDY. The geometries and electronic structures of M₃/GDY have been further analyzed by taking Cu₃/GDY and Pt₃/GDY as two typical examples. Finally, we investigated the catalytic performance of these M₃/GDY SCCs for three kinds of key reactions: ORR, HER, and CO₂ reduction reaction (CO₂RR). The computational results thus provide guidelines for their practical applications as heterogeneous catalysts.

Computational Details

All density functional theory (DFT) calculations were performed with the plane-wave basis sets of 400 eV cutoff kinetic energy to approximate the valence electron densities and projector-augmented wave method to account for the core-valence interaction,⁴⁵ as implemented in the Vienna Ab initio Simulation Package (VASP) code.^{46,47} The spin-polarized Kohn-Sham formalism with gradient-corrected exchange and correlation functional of the Perdew-Burke-Ernzerhof (PBE) flavor was adopted.⁴⁸ The Γ -point-only sampling was used for the Brillouin zone integration for the GDY(2 \times 2)-based models, which were adopted for energy calculations. And a 3 \times 3 \times 1 Brillouin

zone grid sampling was used for the GDY(1×1)-based models, which were adopted for electronic structure analysis. All atoms as well as the lattice parameters **a** and **b** were allowed to relax for geometry optimization. The optimized lattice constant for pristine GDY that we got is $|\mathbf{a}| = |\mathbf{b}| = 9.46 \text{ \AA}$, in good agreement with the previously reported value of 9.48 \AA by Long et al.⁴⁹ The convergence criteria were set to be 10^{-6} eV and $0.01 \text{ eV}/\text{\AA}$ for wavefunction and geometry optimization, respectively.

Free energy correction for all species was performed for ORR, HER, and CO₂RR reactions by VASPKIT.⁵⁰ For free molecules, the ideal gas approximation was assumed. For adsorbates, the contributions from all degrees of freedom to the free energies were treated as vibrations under the harmonic approximation, with unphysically low frequencies reset to a threshold of 60 cm^{-1} , which corresponds to the acoustic translational mode of the six-membered rings in water bulk.^{51,52} All electrochemical calculations were based on Computational Hydrogen Electrode (CHE) model.⁵³ For ORR, we shifted the chemical potential of the electrons by the equilibrium potential of $U = 1.23 \text{ eV}$ [vs standard hydrogen electrode (SHE)], corresponding to the situation where the fuel cell has the maximum potential allowed by thermodynamics.

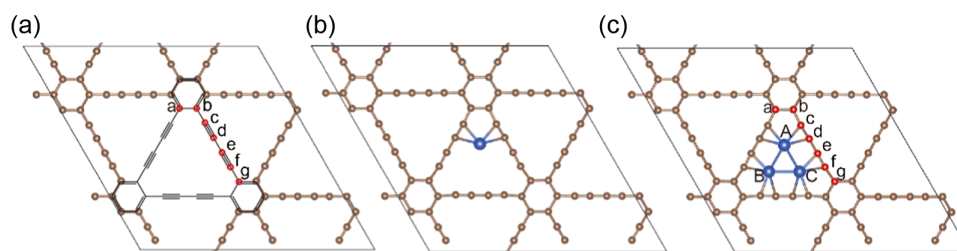
Ab initio molecular dynamics (AIMD) simulations were carried out for all M₃/GDY(2×2). The AIMD calculations were started with the optimized configurations with lattice parameters fixed and were performed for more than 15 ps with a time step of 1 fs. The canonical (NVT) ensemble and Nosé-Hoover thermostats were used with the temperature set to 300 K.^{54,55} AIMD annealing was performed for each M_x/GDY (M = Fe, Co, Ni, Cu, Ru, Rh, Pd, Ag, Os, Ir, Pt, Au; $x = 1-20, 30$) structure. M_x clusters were deposited onto the GDY surface by simulated annealing from 1000 to 100 K in 10 ps, followed by structure optimization. This modeling process was carried out to mimic any experimental deposition procedure that does not necessarily impose precise control on the chemical potential for the target metal element, such as the traditional impregnation and coprecipitation methods. Phonon dispersion was calculated using density-functional perturbation theory,⁵⁶ as implemented in the VASP and analyzed by interfacing with the Phonopy code.⁵⁷

Band structures of GDY, Cu₃/GDY, and Pt₃/GDY were computed along the special line of Γ (0, 0, 0) \rightarrow M (0.5, 0.5, 0) \rightarrow X (0, 0.5, 0) \rightarrow Γ (0, 0, 0) at both PBE and Heyd-Scuseria-Ernzerhof (HSE06) levels.⁵⁸ Band decomposed charge densities were calculated at the Γ point for both the conduction band minimum (CBM) and valence band maximum (VBM) with degenerate bands summed up. Real space wavefunctions of CBM and VBM at the Γ point were extracted by VASPKIT.⁵⁰ The crystal orbital Hamilton population (COHP) analysis was performed with the LOBSTER 3.1.0 package, which reconstructs the orbital-resolved wavefunctions via projection of the delocalized plane waves to localized atomic-like basis sets.^{59,60} The fragment molecular orbital (MO) analysis was performed using spin-restricted DFT with PBE and Slater basis sets of triple-zeta with two polarization functions (TZ2P) as implemented in the Amsterdam Density Functional (ADF) program.⁶¹ The frozen core approximation was applied to C[1s²] and Cu[1s²-2p⁶]. Relativistic effects were introduced by the zero-order regular approximation method. The optimized Cu₃/GDY molecular counterpart and its corresponding fragments (Cu₃ and GDY) were constrained to the D_{3h} symmetry.

Results and Discussion

Stability of M₃/GDY

Scheme 1a shows the structure of pristine GDY (the details are listed in [Supporting Information Table S1](#)), in which the length of the C_c=C_d bond (and its symmetric equivalents) is 1.227 Å, close to that in acetylene (1.20 Å), indicating a typical triple-bond character. There are six C≡C bonds bordering the 18MR-hole of GDY, but only two of them are involved in coordination with metal SA in reported M₁/GDY cases (Scheme 1b).³⁰ Meanwhile the remaining space of an 18MR-hole may accommodate two additional metal atoms coordinated by the rest of the four triple bonds to form M₃/GDY (Scheme 1c). Thus, we investigated the stability of M₃/GDY by comparing the average binding energies E_{bind} ($E_{\text{bind}} = [E(\text{M}_x/\text{GDY}) - x \cdot E(\text{M, bulk}) - E(\text{GDY})]/x$, where x is the number of atoms composing the anchored cluster of metal clusters on GDY, with M covering groups VIII and IB TM elements since they are usually considered as good catalyst candidates.



Scheme 1 | Schematic illustrations of (a) GDY, (b) M₁/GDY, and (c) M₃/GDY.

DOI: [10.31635/ccschem.022.202201796](https://doi.org/10.31635/ccschem.022.202201796)

Citation: CCS Chem. **2023**, 5, 152-163

Link to VoR: <https://doi.org/10.31635/ccschem.022.202201796>

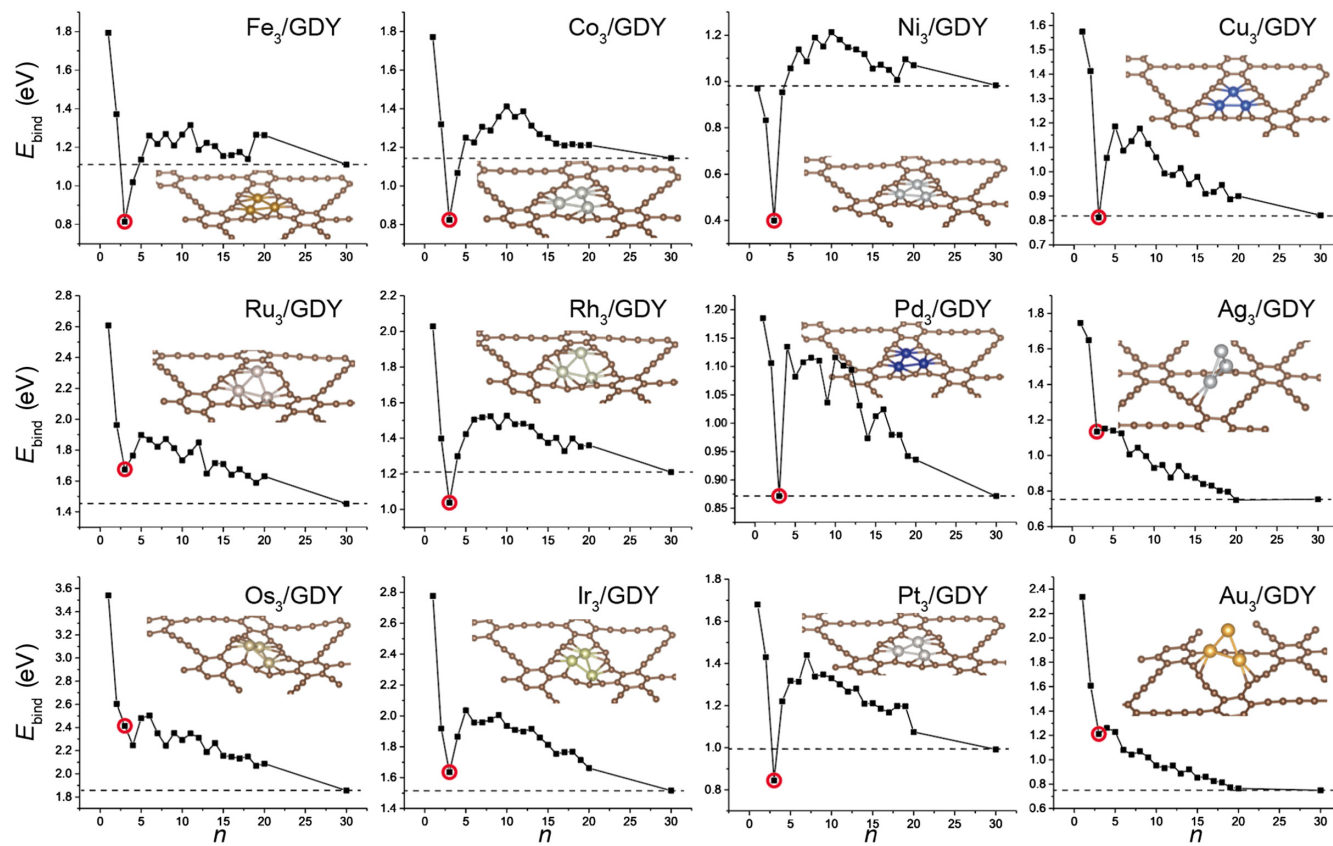


Figure 1 | The average binding energies (E_{bind}) relative to bulk limit, $E_{\text{bind}} = [E(M_x/\text{GDY}) - x \cdot E(\text{M, bulk}) - E(\text{GDY})]/x$, of metal clusters with 1–20 and 30 atoms on GDY. $E(M_x/\text{GDY})$ and $E(\text{GDY})$ is the energy of GDY-supported metal clusters and GDY respectively. x is the number of atoms composing the anchored cluster. $E(\text{M, bulk})$ is the average energy per atom in bulk metal. The black curve shows the E_{bind} changes from M_1 to M_{30} . The points for M_3/GDY are marked in red circles, and their structures are shown in the insets. The dashed line is the reference E_{bind} of M_{30}/GDY , which represents typical $\sim 1\text{ nm}$ nanoparticle. The results show that Fe, Co, Ni, Cu, Rh, and Pt are relatively stable whereas Ru, Pd, Ag, Os, Ir, and Au are not as stable as supported large particles such as M_{30}/GDY .

M_1/GDY can hardly be the most stable case. Instead, it is most unstable for Fe, Co, Cu, Ru, Rh, Os, Ir, Pt, and Au on GDY when compared with other-sized clusters (Figure 1 and Supporting Information Figures S6, S7, S14, and S15). As expected, M_3/GDY is the most stable case for M_x/GDY ($x = 1–10$) cases except Ag, Os, and Au. Taking Cu as an example, the E_{bind} of Cu_1 on GDY is 1.57 eV, but it decreases dramatically to the lowest value of 0.81 eV for Cu_3 . When adding one more Cu atom to Cu_3/GDY , E_{bind} increases to 1.06 eV. E_{bind} peaks at Cu_5 with a value of 1.18 eV and starts to decrease to 0.90 eV at Cu_{20} , due to the formation of more metal–metal bonds. Thus, $x = 3$ becomes a magic number for the thermodynamic stability of these GDY-supported metal clusters. To determine the thermodynamical difference between each cluster from a metal particle, we add a dashed line as reference to M_{30}/GDY , which represents a typical $\sim 1\text{ nm}$ nanoparticle, in each subpanel of Figure 1. The thermodynamically stable M_3/GDY systems lie lower than the dashed line, whereas the metastable or unstable M_3/GDY are above this dashed line. Indeed, Fe, Co, Ni, Cu, Rh, and Pt, are relatively stable,

but Ru, Pd, Ag, Os, Ir, and Au are not as stable as supported large particles such as M_{30}/GDY . The bulk limit of adding an atom of a large metal particle is 0 eV as shown in Figure 1 because the equation of E_{bind} refers to the average energy per atom in bulk metal, $E(\text{M, bulk})$.

AIMD simulations and phonon dispersions of all M_x/GDY cases further characterize their kinetic stability (Supporting Information Figures S1–S5 and S14). In the 15 ps AIMD trajectories, all M_3 clusters remain at the 18MR, except for Ag_3/GDY and Au_3/GDY . The root-mean-square deviations of M_3 clusters are all at low levels with small fluctuations, indicating that no diffusion and decomposition occur within 15 ps. The phonon spectrum, showing no imaginary frequency, further confirms the kinetic stability of Cu_3/GDY (Supporting Information Figure S5). The outstanding stability of M_3/GDY enables the possibility of synthesizing them with the reported EcPW strategy, due to the presence of chemical potential windows that distinguish the trimer cluster form from the other-sized forms anchored on the GDY support.³⁹ The stability of M_3/GDY originates from the specific interactions between the

metal trimer clusters and the GDY support, which can be analyzed and elucidated from geometries and electronic structures discussed in the following sections.

Geometries and electronic structures of M_3 /GDY

Only with M_3 in the plane of GDY may M_3 /GDY retain the D_{3h} symmetry, but most M_3 cannot fit into the 18MR-hole. The optimized M_3 /GDY structures show that only Cu_3 /GDY is of D_{3h} symmetry, and the rest of the M_3 /GDY structures have distortions in both the GDY substrate and M_3 cluster. We summarize the three types of distortions as shown in Figure 2. Type I distortion is with the rotation of both $C\equiv C$ bonds and M_3 within the GDY plane. Type II distortion is with the out-of-plane rotation of M_3 . Type III distortion is also with M_3 moving out of plane but with one metal atom detached from GDY. The cases of Mn, Fe, Ni, Co, Pd, and Pt belong to Type I distortion, which is of C_{3h} symmetry. All type I structures locate in the stable region as shown in Figure 1. This distortion is due to either the mismatch between the 18MR-hole and M_3 or the requirement for specific coordination. The cases of Ru, Rh, Os, and Ir belong to type II distortion, which has no local symmetry. The cases of Ag and Au belong to type III distortion, in which M_3 is out of the GDY plane with only two atoms coordinated to GDY and the remaining atom pushed out and M_3 almost vertical to the GDY plane. The M-M bond lengths of Ag_3 and Au_3 are 2.688 and 2.669 Å, respectively, which are too large to fit in the 18MR. For type II and III structures, except Rh_3 /GDY, all of them are relatively unstable. Compared with type I distortion, types II and III are more mismatched between the 18MR-hole and M_3 and are more unstable.

We further investigate the electronic structures of GDY, Cu_3 /GDY, and Pt_3 /GDY as representative cases. The

electron localization function (ELF) and electrostatic potential maps of GDY (Figures 3a-3c) show that the six triple bonds of 18MR-hole provide localized π electrons (in the GDY plane) at the border, offering perfect anchor sites for TM atoms. In Cu_3 /GDY (Figures 3d-3f), each Cu atom indeed forms two $d\text{-}\pi$ coordination bonds with the localized π systems of $C\equiv C$ bonds in the GDY plane, leaving the π systems perpendicular to the GDY plane intact. And the three 4s orbitals of Cu_3 form a three-center two-electron (3c-2e) bond with the bonding electrons localized above the center of Cu_3 (Figure 3f), which renders the Cu_3 center as a potential nucleophilic SCC. For Pt_3 /GDY, in addition to the $d\text{-}\pi$ coordination, ELF shows a localized red region between Pt and C_c (Figure 3g), implying a typical $d\text{-}\sigma$ covalent bond. Meanwhile, the hybridization of C_c changes from sp to sp^2 -like. $\angle(C_d\text{-}C_e\text{-}C_f)$ decreases from 180° to 145.7° with C_e going away from the Pt_3 cluster (Figures 3h and 3i).

The band structures (Figures 4a-4i and Supporting Information Figure S9) show that the direct band gap of GDY is calculated to be 0.49 and 0.93 eV at PBE and HSE06 levels, respectively, in agreement with previous work.^{49,62} The VBM of GDY is simply composed of the conjugated π system formed by the $C\equiv C$ bonds and benzene rings, with the corresponding π^* orbitals composing the CBM. In Cu_3 /GDY, two new bands appear between the original VBM and CBM, which are composed of the 3c-2e bond by Cu 4s orbitals and the $d\text{-}\pi$ antibonding orbitals. The rest of the 3d bands of Cu_3 are very narrow and localized between -2.0 to -3.2 eV below the Fermi level. The original CBM bands of GDY are partially occupied, due to the charge transfer from Cu_3 to GDY, indicating the metallic character of Cu_3 /GDY. The Bader charge of Cu_3 is $+1.21|e|$, indicating that one 4s electron of Cu_3 is donated to GDY. Thus, the Cu_3 cluster is of $+1$ oxidation state, and the left two 4s bonding electrons forming the 3c-2e bond satisfy the Hückel $[4n + 2]$ electron-counting rule, which is a typical aromatic feature. The analysis of MO interactions between GDY and Cu_3 is presented in Supporting Information Figure S10, which leads to similar conclusions.

For Pt_3 /GDY, the direct band gap is 0.56 and 0.63 eV at PBE and HSE06 levels, respectively. Different from Cu_3 /GDY, there is no new band between the VBM and CBM of GDY. Instead, the 5d orbitals of Pt_3 are mixed into the GDY bands, as shown in the projected band structure and density of states. Such mixing leads to charge transfer from Pt_3 to GDY and strong bonding between Pt and C, reducing the $C\equiv C$ bonds of GDY into double bonds. The integrated crystal orbital Hamilton population (ICOHP) of $C\equiv C$ bonds is reduced from -15.39 to -12.84 eV, and the ICOHP of $C_d\text{-}C_e$ single bonds increases from -11.70 to -12.72 eV (Supporting Information Figure S11). Thus, the bond strengths along the linkage become uniform, which is consistent with the bond length and angle analysis (Supporting Information Figure S8).

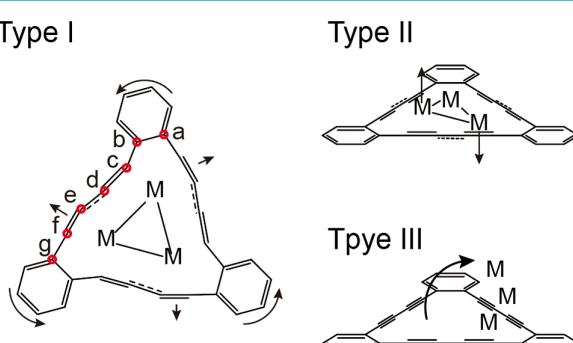


Figure 2 | Type I, II, and III distortions of structures of M_3 /GDY. Type I is the rotation in the GDY plane with local C_{3h} symmetry ($M = Mn, Fe, Ni, Co, Pd$, and Pt). Type II trimers break the mirror symmetry but also bond with 18MR-hole ($M = Ru, Rh, Os$, and Ir). Type III is out of the GDY plane configuration ($M = Ag$ and Au).

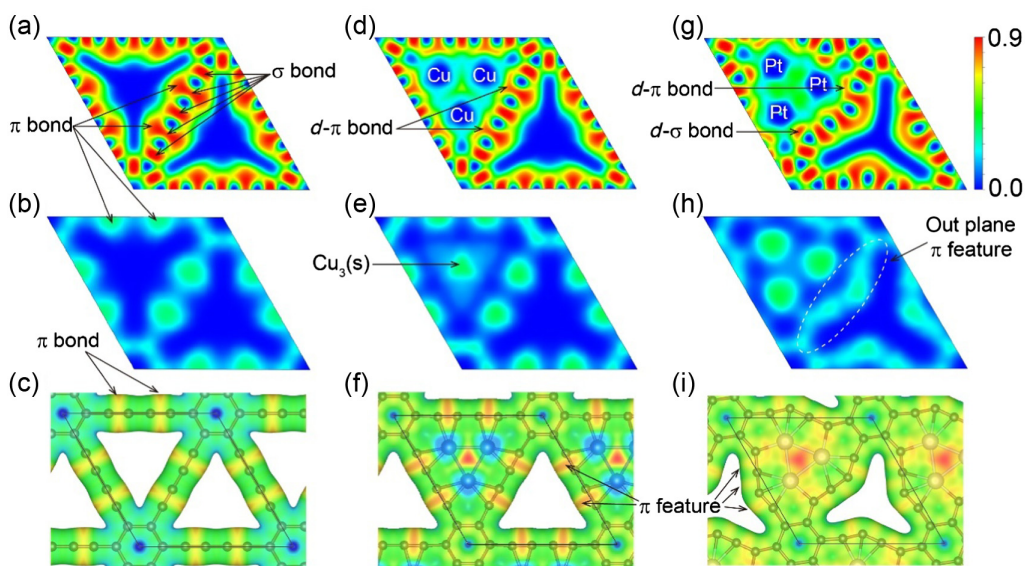


Figure 3 | The 2D contour plots of ELF for (a and b) GDY, (d and e) Cu₃/GDY, and (g and h) Pt₃/GDY at the GDY plane and 1.5 Å above it, respectively. The red/blue region represents electrons accumulation/dispersal. (c, f, and i) The electrostatic-potential-colored charge density isosurfaces at 0.02 |eV/bohr³ for (c) GDY, (f) Cu₃/GDY, and (i) Pt₃/GDY, where the red region is dominated by electrons, and the blue region is dominated by nuclei.

Catalytic performance

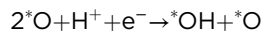
Because of low oxidation states of the metal atoms, the metal clusters of M₃/GDY are electron-rich and thus are good candidate catalysts for reduction reactions (Supporting Information Figure S12). In addition, the GDY substrate can serve as an electron reservoir to buffer the oxidation state change of the M₃ cluster during the catalytic reactions.⁶³ Here, we investigate the ORR, HER, and CO₂RR to demonstrate the catalytic capability of M₃/GDY as a novel series of SCCs.

ORR

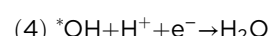
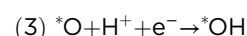
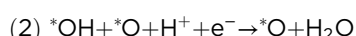
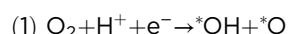
There are two distinct pathways for ORR.^{53,64} One is the associative mechanism, where O₂ is first reduced to *OOH. The other is the dissociative mechanism, where O₂ dissociates first.

The associative mechanism: O₂+H⁺+e⁻→*OOH

The dissociative mechanism: O₂→2*O, followed by



We find that on all M₃/GDY, the dissociative adsorption of O₂ is thermodynamically favored over the molecular adsorption, and the *OOH species is thermodynamically unstable with respect to *O + *OH. Thus, the dissociated mechanism dominates on M₃/GDY, and the four electrochemical steps are:



Note that the dissociation of O₂, which is a chemical step, is integrated into step (1) because we only consider the electrochemical steps here, based on the method by Nørskov et al.⁵³ Figure 5b summarizes the linear relationship between the reaction-free energy ΔG for each electrochemical step and ΔG_{*O} . For step (1), its ΔG increases as the ΔG_{*O} increases. But for the rest of the steps, their ΔG 's have negative slopes with respect to ΔG_{*O} .

Step (3) on all M₃/GDY has the highest ΔG as shown in Figure 5a, and thus it is always the potential limiting step (PLS) that determines the overpotential. Only the overpotential of Au₃/GDY, Ag₃/GDY, Cu₃/GDY, Pt₃/GDY, and Pd₃/GDY are lower than 1 V. Considering that Au₃/GDY and Ag₃/GDY are not stable, only Cu₃/GDY, Pt₃/GDY, and Pd₃/GDY are most likely to be the potential catalysts for ORR with an overpotential of 0.99, 0.94, and 0.70 V, respectively. Then we compare the Cu₃/GDY, Pt₃/GDY, and Pd₃/GDY with Cu(111), Pt(111), and Pd(111) metal surfaces to further investigate the catalytic difference between M₃/GDY and their metal surfaces (Supporting Information Figure S13). The ORR overpotential of Cu(111), Pt(111), and Pd(111) are 0.88, 0.36, and 0.76 V, respectively. It is worth noting that the atomic utilization is 100% for M₃/GDY, but its ORR performance is not as good as the metal surface. The reason is that all M₃ clusters

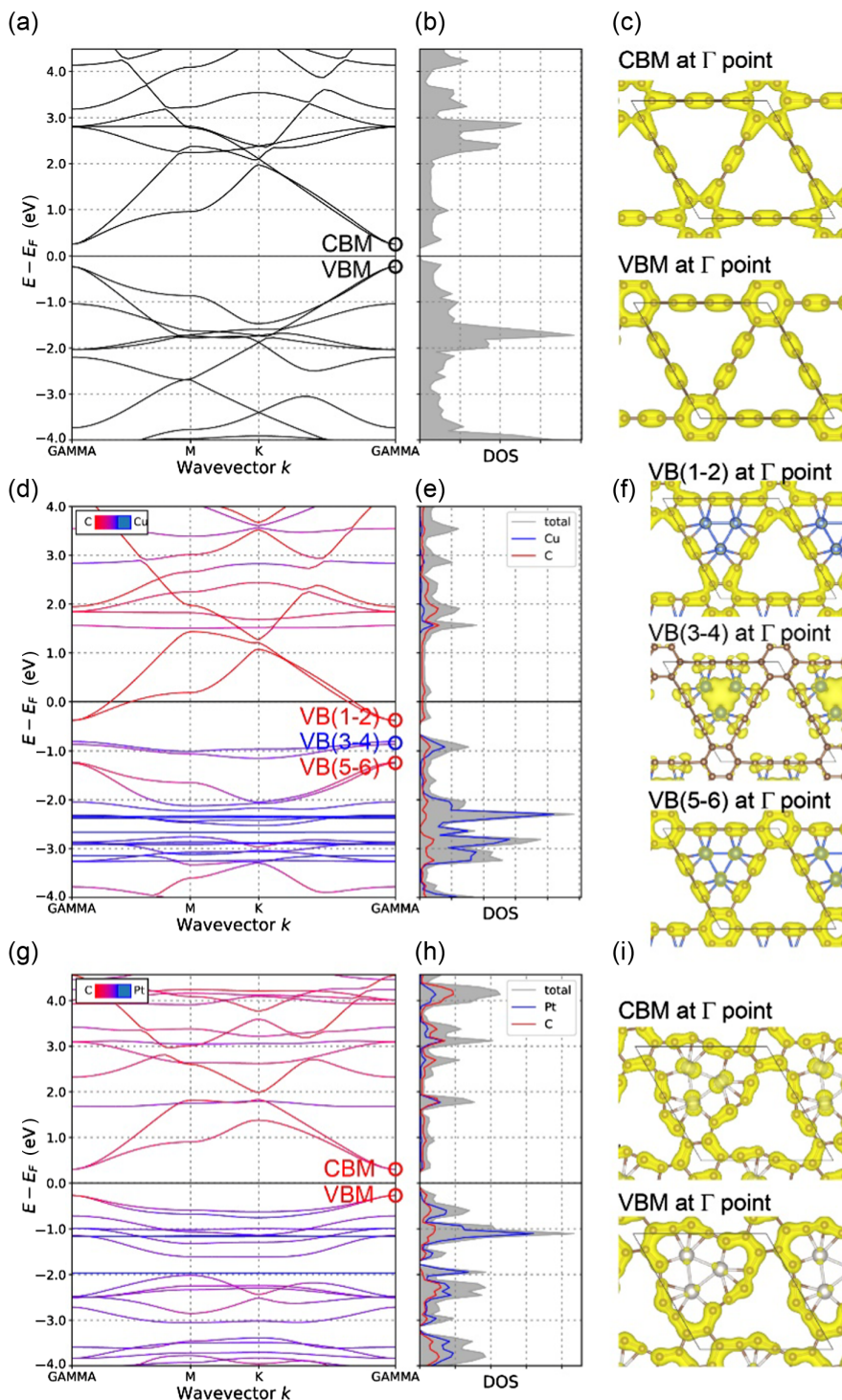


Figure 4 | The band structures (at Γ -M-K- Γ symmetry points) and corresponding projected densities of states at PBE level for (a and b) GDY, (d and e) Cu_3 /GDY, and (g and h) Pt_3 /GDY. The red curves are contributed by C, and the blue curves are contributed by Pt. The isosurface of partial charge density contours of (c) VBM and CBM of GDY, (f) VB (1-6) of Cu_3 /GDY, and (i) VBM and CBM of Pt_3 /GDY.

on GDY are nearly charge-neutral, which will easily reduce O_2 and be poisoned in the first electrochemical step. Such oxygen poison results of ORR on all M_3 /GDY is on the same side of the volcano plot. This is different from the

corresponding series of metal surfaces, among which the Au and Ag surfaces are on the opposite side of the volcano curve to the other metal surfaces, with Pt and Pd close to the top of the volcano.⁵³

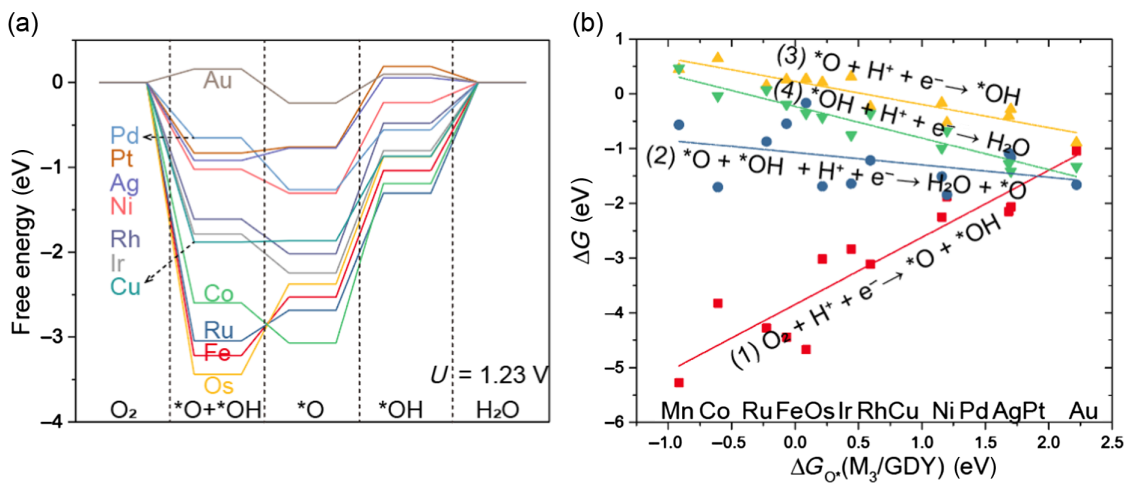


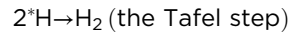
Figure 5 | (a) The free energy diagrams for ORR at $U = 1.23$ V (vs SHE) on M_3/GDY . (b) The linear relationship between ΔG_{O^*} and ΔG for each electrochemical step on M_3/GDY . ΔG is the energy change of each ORR elementary electrochemical steps at $U = 0$ V (vs SHE).

HER

There are two distinct mechanisms for HER, the Volmer-Heyrovsky mechanism and the Volmer-Tafel mechanism.^{65,66} The first elementary reaction of both mechanisms provides the key intermediate $^*\text{H}$ via the Volmer step,



in which the proton source H^+ can be either the solvated proton (e.g., the hydronium ion) or the water molecule. The second step can be either the combination of two $^*\text{H}$ or the further hydrogenation of $^*\text{H}$ by the proton source from the electrolyte,



On M_3/GDY , there is only one threefold hollow site to accommodate one $^*\text{H}$. Thus, only the Volmer-Heyrovsky mechanism is viable, and the PLS is the step with larger ΔG . The predicted overpotentials for HER are lower than 0.05 V on Pt_3/GDY , Os_3/GDY , and Ru_3/GDY . Considering that Ru_3/GDY and Os_3/GDY are not stable, only Pt_3/GDY is potentially a great catalyst candidate (Figure 6a). We compared the activity of HER between M_3/GDY and metal surface as shown in Figure 6b, and the adsorption free energies of the H atom (ΔG_{H^*}) on M_3/GDY and metal bulk

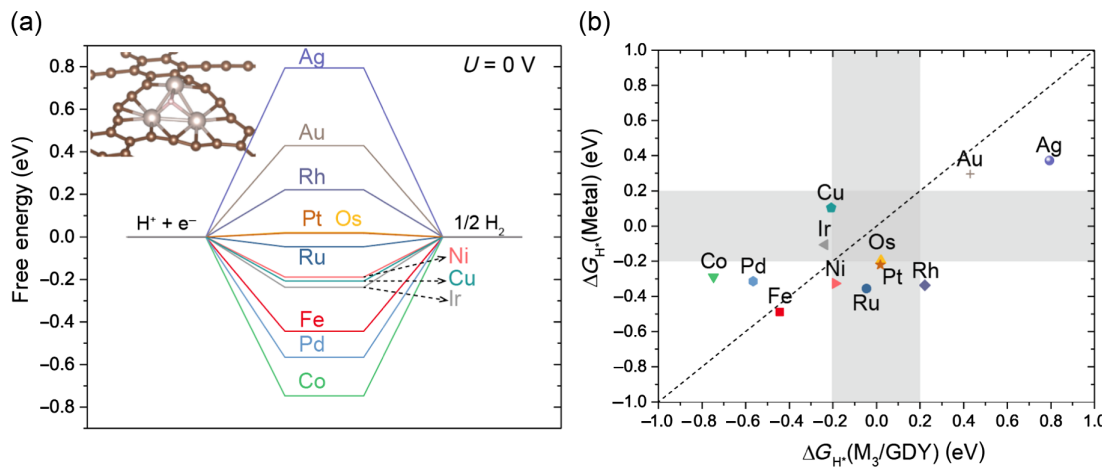


Figure 6 | (a) The free energy diagrams for HER at equilibrium $U = 0$ V (vs SHE) on M_3/GDY . The data are for “standard” conditions corresponding to 1 bar of H_2 and pH 0 at 300 K. The energies for the intermediate adsorbed state are corrected by zero-point energies, entropy, and enthalpy correction at standard thermodynamic conditions. (b) Comparison of ΔG_{H^*} on metal bulk surfaces with those on M_3/GDY , where the gray regions of $|\Delta G_{\text{H}^*}| < 0.2$ eV.

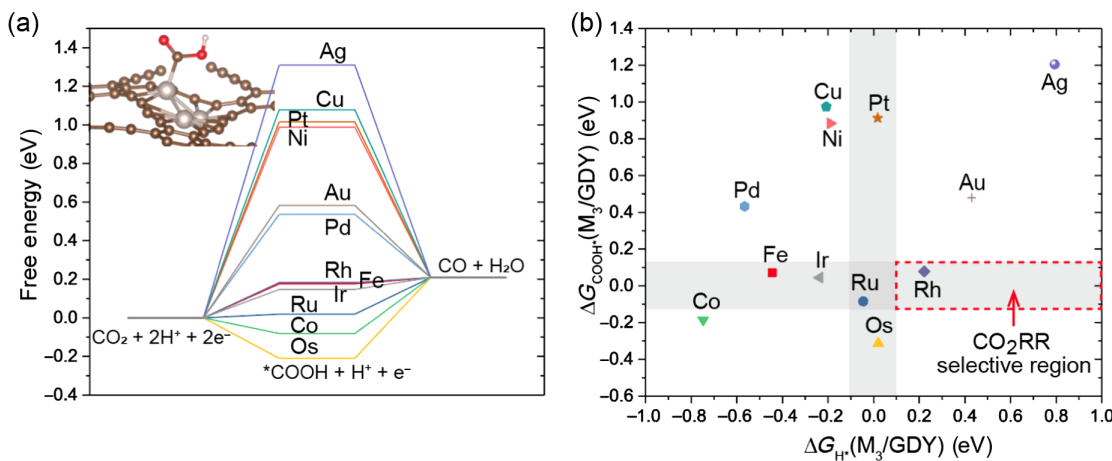
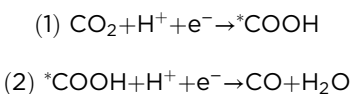


Figure 7 | (a) Free energy diagrams for CO₂RR at U = 0 V (vs SHE) on M₃/GDY. (b) Comparison of ΔG_{H^*} and ΔG_{COOH^*} on M₃/GDY.

surfaces show similar trends. The gray region includes the active sites with $|\Delta G_{H^*}| < 0.2$ eV, which are potential catalyst for industrialization. ΔG_{H^*} on Au₃/GDY, and Ag₃/GDY are too small to drive the Volmer step while ΔG_{H^*} on Co₃/GDY, Pd₃/GDY, and Fe₃/GDY are too large to drive the Heyrovsky step. Pt₃/GDY, Os₃/GDY, and Ru₃/GDY are candidates for HER but can be deactivated with sintering. On the contrary, Cu₃/GDY and Ir₃/GDY will be more active after sintering.

CO₂RR

We also investigate the performance of M₃/GDY for CO₂RR with the mechanism as follows:⁶⁷



and the overall reaction-free energy change is 0.21 eV. Similar to HER, the PLS is the step with larger ΔG . Different from on the metal surface, the *COOH adsorption on partially oxidized M₃ on GDY is not as stable. So, the first CO₂ hydrogenation step is the PLS for Ag₃/GDY, Cu₃/GDY, Pt₃/GDY, Ni₃/GDY, Au₃/GDY, Pd₃/GDY, Rh₃/GDY, Fe₃/GDY, and Ir₃/GDY. But the *COOH hydrogenation step to produce the final product CO is the PLS for Ru₃/GDY, Co₃/GDY, and Os₃/GDY. Figure 7a shows that the predicted overpotentials on Fe₃/GDY, Ir₃/GDY, Ru₃/GDY, and Rh₃/GDY are lower than 0.1 V, implying high activity for CO₂RR. But Fe₃/GDY, Ir₃/GDY, and Ru₃/GDY are not good candidates as CO₂RR catalysts because they suffer from either the preferred adsorptions of *H over *COOH or the competing HER and thus have a selectivity problem. Figure 7b compares ΔG_{H^*} with ΔG_{COOH^*} , where the shadowed regions mark the HER and CO₂RR catalyst candidates with overpotentials lower than 0.1 V. In the left shadowed

region (with Fe₃/GDY and Ir₃/GDY), the *H adsorption is more stable than *COOH, and it may proceed through the formic acid pathway (*H + CO₂ + e⁻ → HCOO⁻).⁶⁷ In the middle shadowed region (with Ru₃/GDY), the competing HER has comparable or higher activity with respect to CO₂RR, leading to poor selectivity. In the right shadowed region (with Rh₃/GDY), the high activity for CO₂RR dominates that for HER, and thus Rh₃/GDY is an optimal candidate for highly efficient and selective CO₂RR.

In summary, based on the CHE model,⁵³ we calculated the free energy of intermediates for ORR, HER, and CO₂RR. We found that Cu₃/GDY, Pt₃/GDY, and Pd₃/GDY are potential catalyst candidates for ORR, Pt₃/GDY is a potential candidate for HER, and Rh₃/GDY is a potential candidate for CO₂RR. It should be noted that the solvation effect, kinetic barrier, and constant potential are not considered in this work. Thus, this electrochemical investigation aims at demonstrating the concept while further rigorous calculations and experimental verification are needed in the future.

Summary

By investigating the thermodynamic properties, we predict that the metal trimer cluster form anchored on GDY (i.e., M₃/GDY) is most stable among all forms including the previously reported single-atom M₁/GDY for Fe, Co, Ni, Cu, Ru, Rh, Pd, Ir, and Pt. This finding lays the foundation for the synthesis of these M₃/GDY with our proposed EcPW strategy. We have further investigated the geometric and electronic structures to elucidate the specific interactions between the M₃ single clusters, and the GDY support that result in the extraordinary stability of M₃/GDY. More importantly, we propose this series of stable M₃/GDY as a novel and promising kind of SCCs with great potential for efficient and atomically precise heterogenous catalysis.

We have demonstrated their catalytic performance for ORR, HER, and CO₂RR, which can provide guidelines for design graphdiyne-based SCCs for practical applications.

Supporting Information

Supporting Information is available and includes the details of the AIMD simulations, phonon spectra, structure distortions analysis, MOs, COHP, and d-band center data.

Conflict of Interest

There is no conflict of interest to report.

Preprint Acknowledgment

Research presented in this article was posted on a preprint server prior to publication in *CCS Chemistry*. The corresponding preprint article can be found here: <https://doi.org/10.26434/chemrxiv.13160282.v1>.

Acknowledgments

This work was financially supported by the National Natural Science Foundation of China (grant no. 22033005 to J.L. and grant no. 21903047 to H.X.). The support of Guangdong Provincial Key Laboratory of Catalysis (grant no. 2020B121201002) is also acknowledged. The calculations were performed using the supercomputers at Tsinghua National Laboratory for Information Science and Technology, the Computational Chemistry Laboratory of the Department of Chemistry under the Tsinghua Xuetang Talents Program, and the Supercomputer Center of the Southern University of Science and Technology.

References

1. Qiao, B.; Wang, A.; Yang, X.; Allard, L. F.; Jiang, Z.; Cui, Y.; Liu, J.; Li, J.; Zhang, T. Single-Atom Catalysis of CO Oxidation Using Pt₁/FeO_x. *Nat. Chem.* **2011**, *3*, 634–641.
2. Yang, X.-F.; Wang, A.; Qiao, B.; Li, J.; Liu, J.; Zhang, T. Single-Atom Catalysts: A New Frontier in Heterogeneous Catalysis. *Acc. Chem. Res.* **2013**, *46*, 1740–1748.
3. Liu, J. Catalysis by Supported Single Metal Atoms. *ACS Catal.* **2017**, *7*, 34–59.
4. Wang, A.; Li, J.; Zhang, T. Heterogeneous Single-Atom Catalysis. *Nat. Rev. Chem.* **2018**, *2*, 65–81.
5. Liu, J.-C.; Tang, Y.; Li, J.; Wang, Y.-G.; Zhang, T. Theoretical Understanding of the Stability of Single-Atom Catalysts. *Natl. Sci. Rev.* **2018**, *5*, 638–641.
6. Liu, L.; Corma, A. Metal Catalysts for Heterogeneous Catalysis: From Single Atoms to Nanoclusters and Nanoparticles. *Chem. Rev.* **2018**, *118*, 4981–5079.
7. Crabtree, R. H. Resolving Heterogeneity Problems and Impurity Artifacts in Operationally Homogeneous Transition Metal Catalysts. *Chem. Rev.* **2012**, *112*, 1536–1554.
8. Rong, H.; Ji, S.; Zhang, J.; Wang, D.; Li, Y. Synthetic Strategies of Supported Atomic Clusters for Heterogeneous Catalysis. *Nat. Commun.* **2020**, *11*, 5884.
9. Michaelides, A.; Hu, P. Insight into Microscopic Reaction Pathways in Heterogeneous Catalysis. *J. Am. Chem. Soc.* **2000**, *122*, 9866–9867.
10. Tyo, E. C.; Vajda, S. Catalysis by Clusters with Precise Numbers of Atoms. *Nat. Nanotech.* **2015**, *10*, 577–588.
11. Ji, S.; Chen, Y.; Fu, Q.; Chen, Y.; Dong, J.; Chen, W.; Li, Z.; Wang, Y.; Gu, L.; He, W.; Chen, C.; Peng, Q.; Huang, Y.; Duan, X.; Wang, D.; Draxl, C.; Li, Y. Confined Pyrolysis within Metal-Organic Frameworks to Form Uniform Ru₃ Clusters for Efficient Oxidation of Alcohols. *J. Am. Chem. Soc.* **2017**, *139*, 9795–9798.
12. Huang, H.; Zhao, Y.; Bai, Y.; Li, F.; Zhang, Y.; Chen, Y. Conductive Metal-Organic Frameworks with Extra Metallic Sites as an Efficient Electrocatalyst for the Hydrogen Evolution Reaction. *Adv. Sci.* **2020**, *7*, 2000012.
13. Zheng, F.; Zhang, C.; Gao, X.; Du, C.; Zhuang, Z.; Chen, W. Immobilizing Pd Nanoclusters into Electronically Conductive Metal-Organic Frameworks as Bi-Functional Electrocatalysts for Hydrogen Evolution and Oxygen Reduction Reactions. *Electrochim. Acta* **2019**, *306*, 627–634.
14. Wang, J.; Huang, Z.; Liu, W.; Chang, C.; Tang, H.; Li, Z.; Chen, W.; Jia, C.; Yao, T.; Wei, S.; Wu, Y.; Li, Y. Design of N-Coordinated Dual-Metal Sites: A Stable and Active Pt-Free Catalyst for Acidic Oxygen Reduction Reaction. *J. Am. Chem. Soc.* **2017**, *139*, 17281–17284.
15. Jiao, J.; Lin, R.; Liu, S.; Cheong, W.-C.; Zhang, C.; Chen, Z.; Pan, Y.; Tang, J.; Wu, K.; Hung, S.-F.; Chen, H. M.; Zheng, L.; Lu, Q.; Yang, X.; Xu, B.; Xiao, H.; Li, J.; Wang, D.; Peng, Q.; Chen, C.; Li, Y. Copper Atom-Pair Catalyst Anchored on Alloy Nanowires for Selective and Efficient Electrochemical Reduction of CO₂. *Nat. Chem.* **2019**, *11*, 222–228.
16. Yamamoto, K.; Imaoka, T.; Tanabe, M.; Kambe, T. New Horizon of Nanoparticle and Cluster Catalysis with Dendrimers. *Chem. Rev.* **2020**, *120*, 1397–1437.
17. Zhang, S.; Nguyen, L.; Liang, J. X.; Shan, J.; Liu, J.; Frenkel, A. I.; Patlolla, A.; Huang, W.; Li, J.; Tao, F. Catalysis on Singly Dispersed Bimetallic Sites. *Nat. Commun.* **2015**, *6*, 7938.
18. Lei, Y.; Mehmood, F.; Lee, S.; Greeley, J.; Lee, B.; Seifert, S.; Winans, R. E.; Elam, J. W.; Meyer, R. J.; Redfern, P. C.; Teschner, D.; Schlogl, R.; Pellin, M. J.; Curtiss, L. A.; Vajda, S. Increased Silver Activity for Direct Propylene Epoxidation via Subnanometer Size Effects. *Science* **2010**, *328*, 224–228.
19. Ma, X.-L.; Liu, J.-C.; Xiao, H.; Li, J. Surface Single-Cluster Catalyst for N₂-to-NH₃ Thermal Conversion. *J. Am. Chem. Soc.* **2018**, *140*, 46–49.
20. Liu, J.-C.; Ma, X.-L.; Li, Y.; Wang, Y.-G.; Xiao, H.; Li, J. Heterogeneous Fe₃ Single-Cluster Catalyst for Ammonia Synthesis via an Associative Mechanism. *Nat. Commun.* **2018**, *9*, 1610.
21. Grundner, S.; Markovits, M. A. C.; Li, G.; Tromp, M.; Pidko, E. A.; Hensen, E. J. M.; Jentys, A.; Sanchez-Sanchez, M.;

- Lercher, J. A. Single-Site Trinuclear Copper Oxygen Clusters in Mordenite for Selective Conversion of Methane to Methanol. *Nat. Commun.* **2015**, *6*, 7546.
22. Li, Y.; Xu, L.; Liu, H.; Li, Y. Graphdiyne and Graphyne: From Theoretical Predictions to Practical Construction. *Chem. Soc. Rev.* **2014**, *43*, 2572–2586.
23. Gao, X.; Liu, H.; Wang, D.; Zhang, J. Graphdiyne: Synthesis, Properties, and Applications. *Chem. Soc. Rev.* **2019**, *48*, 908–936.
24. Huang, C.; Li, Y.; Wang, N.; Xue, Y.; Zuo, Z.; Liu, H.; Li, Y. Progress in Research into 2D Graphdiyne-Based Materials. *Chem. Rev.* **2018**, *118*, 7744–7803.
25. Haley, M. M.; Brand, S. C.; Pak, J. J. Carbon Networks Based on Dehydrobenzoannulenes: Synthesis of Graphdiyne Substructures. *Angew. Chem. Int. Ed. Engl.* **1997**, *36*, 836–838.
26. Pan, Q.; Chen, S.; Wu, C.; Shao, F.; Sun, J.; Sun, L.; Zhang, Z.; Man, Y.; Li, Z.; He, L. Direct Synthesis of Crystalline Graphtetrayne—A New Graphyne Allotrope. *CCS Chem.* **2021**, *3*, 1368–1375.
27. Zuo, Z.; Li, Y. Emerging Electrochemical Energy Applications of Graphdiyne. *Joule* **2019**, *3*, 899–903.
28. Zhao, Y.; Tang, H.; Yang, N.; Wang, D. Graphdiyne: Recent Achievements in Photo- and Electrochemical Conversion. *Adv. Sci. (Weinh.)* **2018**, *5*, 1800959.
29. Xue, Y.; Huang, B.; Yi, Y.; Guo, Y.; Zuo, Z.; Li, Y.; Jia, Z.; Liu, H.; Li, Y. Anchoring Zero Valence Single Atoms of Nickel and Iron on Graphdiyne for Hydrogen Evolution. *Nat. Commun.* **2018**, *9*, 1460.
30. Li, X.; Xing, D. Systematic Theoretical Study of Electronic Structures and Stability of Transition-Metal-Adsorbed Graphdiyne Clusters. *J. Mater. Chem. C* **2019**, *123*, 8843–8850.
31. Hui, L.; Xue, Y.; Yu, H.; Liu, Y.; Fang, Y.; Xing, C.; Huang, B.; Li, Y. Highly Efficient and Selective Generation of Ammonia and Hydrogen on a Graphdiyne-Based Catalyst. *J. Am. Chem. Soc.* **2019**, *141*, 10677–10683.
32. Xu, G.; Wang, R.; Ding, Y.; Lu, Z.; Ma, D.; Yang, Z. First-Principles Study on the Single Ir Atom Embedded Graphdiyne: An Efficient Catalyst for CO Oxidation. *J. Phys. Chem. C* **2018**, *122*, 23481–23492.
33. He, T.; Matta, S. K.; Du, A. Single Tungsten Atom Supported on N-Doped Graphyne as a High-Performance Electrocatalyst for Nitrogen Fixation Under Ambient Conditions. *Phys. Chem. Chem. Phys.* **2019**, *21*, 1546–1551.
34. Yin, X. P.; Wang, H. J.; Tang, S. F.; Lu, X. L.; Shu, M.; Si, R.; Lu, T. B. Engineering the Coordination Environment of Single-Atom Platinum Anchored on Graphdiyne for Optimizing Electrocatalytic Hydrogen Evolution. *Angew. Chem. Int. Ed. Engl.* **2018**, *57*, 9382–9386.
35. Gao, Y.; Cai, Z.; Wu, X.; Lv, Z.; Wu, P.; Cai, C. Graphdiyne-Supported Single-Atom-Sized Fe Catalysts for the Oxygen Reduction Reaction: DFT Predictions and Experimental Validations. *ACS Catal.* **2018**, *8*, 10364–10374.
36. Li, X.; Li, S. Investigations of Electronic and Nonlinear Optical Properties of Single Alkali Metal Adsorbed Graphene, Graphyne and Graphdiyne Systems by First-Principles Calculations. *J. Mater. Chem. C* **2019**, *7*, 1630–1640.
37. He, T.; Matta, S. K.; Will, G.; Du, A. Transition-Metal Single Atoms Anchored on Graphdiyne as High-Efficiency Electrocatalysts for Water Splitting and Oxygen Reduction. *Small Methods* **2019**, *3*, 1800419.
38. Seif, A.; López, M. J.; Granja-DelRío, A.; Azizi, K.; Alonso, J. A. Adsorption and Growth of Palladium Clusters on Graphdiyne. *Phys. Chem. Chem. Phys.* **2017**, *19*, 19094–19102.
39. Liu, J.-C.; Xiao, H.; Li, J. Constructing High-Loading Single-Atom/Cluster Catalysts via an Electrochemical Potential Window Strategy. *J. Am. Chem. Soc.* **2020**, *142*, 3375–3383.
40. Ma, D.; Zeng, Z.; Liu, L.; Huang, X.; Jia, Y. Computational Evaluation of Electrocatalytic Nitrogen Reduction on TM Single-, Double-, and Triple-Atom Catalysts (TM = Mn, Fe, Co, Ni) Based on Graphdiyne Monolayers. *J. Phys. Chem. C* **2019**, *123*, 19066–19076.
41. Zhang, H.; Xia, Y.; Bu, H.; Wang, X.; Zhang, M.; Luo, Y.; Zhao, M. Graphdiyne: A Promising Anode Material for Lithium Ion Batteries with High Capacity and Rate Capability. *J. Appl. Phys.* **2013**, *113*, 044309.
42. Qi, H.; Yu, P.; Wang, Y.; Han, G.; Liu, H.; Yi, Y.; Li, Y.; Mao, L. Graphdiyne Oxides as Excellent Substrate for Electroless Deposition of Pd Clusters with High Catalytic Activity. *J. Am. Chem. Soc.* **2015**, *137*, 5260–5263.
43. Xing, D.-H.; Xu, C.-Q.; Wang, Y.-G.; Li, J. Heterogeneous Single Cluster Catalysts for Selective Semi-Hydrogenation of Acetylene with Graphdiyne-Supported Triatomic Clusters. *J. Phys. Chem. C* **2019**, *123*, 10494–10500.
44. Ikuno, T.; Grundner, S.; Jentys, A.; Li, G.; Pidko, E.; Fulton, J.; Sanchez-Sanchez, M.; Lercher, J. A. Formation of Active Cu-Oxo Clusters for Methane Oxidation in Cu-Exchanged Mordenite. *J. Phys. Chem. C* **2019**, *123*, 8759–8769.
45. Kresse, G.; Joubert, D. From Ultrasoft Pseudopotentials to the Projector Augmented-Wave Method. *Phys. Rev. B: Condens. Matter Mater. Phys.* **1999**, *59*, 1758.
46. Kresse, G.; Furthmüller, J. Efficient Iterative Schemes for Ab Initio Total-Energy Calculations Using a Plane-Wave Basis Set. *Phys. Rev. B: Condens. Matter Mater. Phys.* **1996**, *54*, 11169.
47. Kresse, G.; Furthmüller, J. Efficiency of Ab-Initio Total Energy Calculations for Metals and Semiconductors Using a Plane-Wave Basis Set. *Comput. Mater. Sci.* **1996**, *6*, 15–50.
48. Perdew, J. P.; Burke, K.; Ernzerhof, M. Generalized Gradient Approximation Made Simple. *Phys. Rev. Lett.* **1996**, *77*, 3865.
49. Long, M.; Tang, L.; Wang, D.; Li, Y.; Shuai, Z. Electronic Structure and Carrier Mobility in Graphdiyne Sheet and Nanoribbons: Theoretical Predictions. *ACS Nano* **2011**, *5*, 2593–2600.
50. Wang, V.; Xu, N.; Liu, J.-C.; Tang, G.; Geng, W.-T. VASP-KIT: A User-Friendly Interface Facilitating High-Throughput Computing and Analysis Using VASP Code. *Comput. Phys. Commun.* **2021**, *267*, 108033.
51. Liu, H.; Wang, Y.; Bowman, J. M. Vibrational Analysis of an Ice Ih Model from 0 to 4000 cm⁻¹ Using the Ab Initio WHBB Potential Energy Surface. *J. Phys. Chem. B* **2013**, *117*, 10046–10052.
52. Bertie, J. E.; Whalley, E. Optical Spectra of Orientationally Disordered Crystals. II. Infrared Spectrum of Ice Ih and Ice Ic from 360 to 50 cm⁻¹. *J. Chem. Phys.* **1967**, *46*, 1271–1284.

53. Nørskov, J. K.; Rossmeisl, J.; Logadottir, A.; Lindqvist, L.; Kitchin, J. R.; Bligaard, T.; Jónsson, H. Origin of the Overpotential for Oxygen Reduction at a Fuel-Cell Cathode. *J. Phys. Chem. B* **2004**, *108*, 17886–17892.
54. Nosé, S. A Unified Formulation of the Constant Temperature Molecular Dynamics Methods. *J. Chem. Phys.* **1984**, *81*, 511.
55. Hoover, W. G. Canonical Dynamics: Equilibrium Phase-Space Distributions. *Phys. Rev. A* **1985**, *31*, 1695–1697.
56. Baroni, S.; de Gironcoli, S.; Dal Corso, A.; Giannozzi, P. Phonons and Related Crystal Properties from Density-Functional Perturbation Theory. *Rev. Mod. Phys.* **2001**, *73*, 515–562.
57. Togo, A.; Tanaka, I. First Principles Phonon Calculations in Materials Science. *Scripta Mater.* **2015**, *108*, 1–5.
58. Heyd, J.; Scuseria, G. E.; Ernzerhof, M. Erratum: “Hybrid functionals based on a screened Coulomb potential” [J. Chem. Phys. 118, 8207 (2003)]. *J. Chem. Phys.* **2006**, *124*, 219906.
59. Maintz, S.; Deringer, V. L.; Tchougréeff, A. L.; Dronskowski, R. LOBSTER: A Tool to Extract Chemical Bonding from Plane-Wave Based DFT. *J. Comput. Chem.* **2016**, *37*, 1030–1035.
60. Deringer, V. L.; Tchougréeff, A. L.; Dronskowski, R. Crystal Orbital Hamilton Population (COHP) Analysis as Projected from Plane-Wave Basis Sets. *J. Phys. Chem. A* **2011**, *115*, 5461–5466.
61. ADF2019, S. *Theoretical Chemistry*; Vrije Universiteit: Amsterdam, The Netherlands, <http://www.scm.com>
62. Tan, X.; Shao, H.; Hu, T.; Liu, G.; Jiang, J.; Jiang, H. High Thermoelectric Performance in Two-Dimensional Graphyne Sheets Predicted by First-Principles Calculations. *Phys. Chem. Chem. Phys.* **2015**, *17*, 22872–22881.
63. Li, X. F.; Li, Q. K.; Cheng, J.; Liu, L.; Yan, Q.; Wu, Y.; Zhang, X. H.; Wang, Z. Y.; Qiu, Q.; Luo, Y. Conversion of Dinitrogen to Ammonia by FeN₃-Embedded Graphene. *J. Am. Chem. Soc.* **2016**, *138*, 8706–8709.
64. Seh, Z. W.; Kibsgaard, J.; Dickens, C. F.; Chorkendorff, I.; Norskov, J. K.; Jaramillo, T. F. Combining Theory and Experiment in Electrocatalysis: Insights into Materials Design. *Science* **2017**, *355*, eaad4998.
65. Rice, P. S.; Liu, Z.-P.; Hu, P. Hydrogen Coupling on Platinum Using Artificial Neural Network Potentials and DFT. *J. Phys. Chem. Lett.* **2021**, *12*, 10637–10645.
66. de Chalvo, M. G.; Chalvo, A. Hydrogen Evolution Reaction: Analysis of the Volmer-Heyrovsky-Tafel Mechanism with a Generalized Adsorption Model. *J. Electroanal. Chem.* **1994**, *372*, 209–223.
67. Cheng, T.; Xiao, H.; Goddard, W. A. Reaction Mechanisms for the Electrochemical Reduction of CO₂ to CO and Formate on the Cu(100) Surface at 298K from Quantum Mechanics Free Energy Calculations with Explicit Water. *J. Am. Chem. Soc.* **2016**, *138*, 13802–13805.